Consistent wide-range equation of state of silicon by a unified first-principles method

Chang Gao,[1,2] Xing Liu,[3,2] Shen Zhang,[4,5,*] Wei Kang,[5,†] Ping Zhang,[5,6] and X. T. He[5,6,‡]

[1]*School of Science, Wuhan University of Technology, Wuhan, Hubei 430070, China*
[2]*HEDPS, Center for Applied Physics and Technology and School of Physics, Peking University, Beijing 100871, China*
[3]*China Institute of Nuclear Industry Strategy, Beijing 100048, China*
[4]*Department of Nuclear Science and Technology, National University of Defense Technology, Changsha, Hunan 410073, China*
[5]*HEDPS, Center for Applied Physics and Technology and College of Engineering, Peking University, Beijing 100871, China*
[6]*Institute of Applied Physics and Computational Mathematics, Beijing 100088, China*

(Received 29 January 2023; revised 12 April 2023; accepted 13 April 2023; published 26 April 2023)

Using a unified method of the extended first-principles molecular dynamics, we report a wide-range (density $\rho = 2.329$–18.632 g/cm^3, temperature $T = 1.00 \times 10^4$–1.29×10^8 K) equation of state (EOS) and principal Hugoniot of silicon, which agree well with experimental results, and then evaluate the precision of the results of first-principles calculations and a universal database. Moreover, we investigate the effects of finite-temperature exchange-correlation functionals and emphasize their importance and necessity in the warm dense matter regime, although it vanishes in the nondegenerate and fully degenerate limits. Finally, we show the ionic radial distribution function and density of electronic states to study the evolution of warm dense Si towards the classic plasma limit along its principal Hugoniot. The established standard theoretical EOS table of Si provides a benchmark for the development of high-precision first-principles methods and may improve radiation-hydrodynamics simulations of inertial confinement fusion and deepen the understanding of high-energy-density physics.

DOI: 10.1103/PhysRevB.107.165150

I. INTRODUCTION

Silicon has been extensively studied in several fields because of its rich phase diagram and complex characters. In modern industry, Si occupies a key position due to its excellent semiconductor performance. Solid Si was discovered to transform into novel phases at high pressure and temperature. In condensed matter physics, high-pressure phases, metallic phases [1–6], and metastable end phases [7] have been well investigated to explore the phase diagram of Si. In geophysics, Si is the second richest element in Earth's crust and is regarded as one of the most likely light elements in Earth's inner and outer core. The equation of state (EOS) and sound velocity of Fe-Si alloys are fundamental parameters to determine the composition of Earth's core [8–12]. In planetary science, phase transitions and the structural change processes of silicon compounds, including silica and silicates, are of great importance for understanding the structure and evolution of planets and exoplanets [13]. In astrophysics, Si widely participates in important chemical reactions in interstellar space at astrophysical conditions [14,15]. At higher temperatures and pressures in shock experiments, solid Si turns into a fluid state or plasma state, and silica is widely used as a window to obtain the EOS of other materials [16,17]. In inertial confinement fusion (ICF) [18,19], Si is employed as a dopant in the ablator of the ignition target to reduce the preheating effect [20,21]. Hence, an accurate EOS and phase diagram for Si under various physical conditions have broad interest for a number of research fields.

However, obtaining the material properties of Si under extreme conditions, i.e., extremely high pressures and temperatures, has been a formidable task, owing to the limitation of even state-of-the-art experimental techniques and calculation methods. Abundant phenomena with complex underlying physics, such as bond reconstruction, ionization potential depression, and phase transition, are expected to occur under extreme conditions, especially in the warm dense matter regime [22–24]. Both experimental and theoretical physicists are endeavoring to expand the border of knowledge under extreme conditions.

For shock experiments, the first experimental measurement of EOS was carried out in the 1960s by explosive-driven shock [25] pushing pressure up to ∼200 GPa. Following studies [26,27] on the shock compression properties of Si provided more data along principal Hugoniot curves in the 1970s and 1980s. More recently, a laser-driven experiment [28] found the anomalous elastic response phenomenon of compressed single crystals of Si in 2001. The latest milestone of Henderson *et al.* [29] on laser shock experiments found a phase transition of fluid-state Si corresponding to an increase in ionic coordination and average ionization and achieved Hugoniot and sound speed data up to 2100 GPa.

For theoretical calculations, early researches on the behavior of Si in solid and liquid phases under shock compression were carried out using classical molecular dynamics (MD) [30–32]. Afterward, first-principles methods without empirical parameters were introduced for a more accurate description of atomic interactions by solving quantum Schrödinger-like equations with different physical

*shenzhang@nudt.edu.cn
†weikang@pku.edu.cn
‡xthe@iapcm.ac.cn

approximations, such as the Kohn-Sham molecular dynamics (KSMD) method [33–35], the orbital-free molecular dynamics (OFMD) method [36], and the path-integral Monte Carlo (PIMC) method [37,38]. An EOS of Si at pressures less than 10 Mbar, i.e., states in the range of solid crystals to liquid states located in the phase diagram, was obtained using KSMD calculations [39,40]. For more extreme conditions, recently developed high-temperature first-principles methods, i.e., OFMD and PIMC, have the ability to calculate the EOS and shock properties of Si with pressures higher than 100 Mbar. First-principles EOS tables of Si ranging from solid state to ideal plasma were established by combining the KSMD and high-temperature first-principles methods [41,42] and were then implemented in radiation-hydrodynamics simulations of ICF [43], which helps to verify the feasibility of the fusion ignition scheme.

All of the above first-principles methods have their advantages and disadvantages according to different treatments of electrons. The KSMD method can give precise electronic structure information based on density functional theory, but it has the problem of dealing with a large amount of high-energy excited electrons due to the increase in temperature [44,45]. Consequently, the OFMD method adopts well-designed kinetic energy functionals to replace the single-particle kinetic energy operator in the KSMD method [46–50] and remarkably improves computational efficiency and simulation size. However, it leads to inconsistent results at relatively low temperatures compared with the KSMD method, especially in describing the electron's inner shell structure. An alternative solution is the PIMC method, based on the framework of the thermal path-integral density matrix in combination with Monte Carlo sampling [38,41,51–53]. The "Fermion sign problem" that restricts the applicable region of PIMC was solved by introducing the Hartree-Fock nodes instead of previous free-particle nodes in recent efforts [41], making the PIMC method one of the most efficient and accurate first-principles methods at high temperatures. As a result of the limitations of the validity boundaries of the above methods, the EOS and phase diagram obtained from different methods are not always consistent for a wide range of conditions, i.e., from ambient to extremely high temperature and pressure conditions. Therefore, a unified first-principles method that fully considers significant physical effects is essential for studying warm dense matter and high-energy-density physics.

The recently developed extended first-principles molecular dynamics (ext-FPMD) of Zhang *at al.* [54] provides a unified method to get accurate thermodynamic quantities at high temperatures by dealing with the wave function of high-energy electrons as plane waves. The ext-FPMD method not only inherts the same high accuracy as the KSMD method naturally but also provides the wave functions of inner shell electrons, whereas the OFMD method and the PIMC method do not. Thus, calculations that cover the entire phase diagram and do not divide it into several parts for which valid corresponding methods must be utilized separately can be done with only one method, i.e., the ext-FPMD method. Previous studies [55–60] reported its broad applications to low-Z and middle-Z materials at temperatures ranging from ambient temperature to a few thousand eV.

In this paper, we obtain a consistent first-principles data set for a wide-range ($\rho = 2.329$–18.632 g/cm^3, $T = 1.00 \times 10^4$–1.29×10^8 K) EOS and principal Hugoniot of Si using the ext-FPMD method. As a benchmark for the EOS of Si at high temperatures, the results are comprehensively compared with existing first-principles calculations and universal databases. Along the principal Hugoniot curve, we observe the thermal ionization process of inner shell electrons and the influence of the electronic shell structure effect on the shock compression curves. Moreover, the effect of finite-temperature exchange-correlation (FTXC) functionals on the EOS is investigated in the whole phase diagram, emphasizing the importance and necessity of FTXC in the warm dense matter regime. Finally, we reveal the microscopic structure information of ions and electrons extracted using the ext-FPMD method and obtain the radial distribution functions (RDFs) and the density of electronic states (DOS) at fourfold density. It thus helps to verify the accuracy and efficiency of existing theoretical simulations and establish the standard EOS database.

The rest of this paper is composed of three sections. In Sec. II, we briefly review the ext-FPMD method and provide computational details. In Sec. III, we discuss simulation results for the EOS, principal Hugoniot, RDF, and DOS of Si under extreme conditions of temperature and pressure. In addition, we reveal the effect of the FTXC functionals. In Sec. IV, we give a summary.

II. METHODOLOGY AND COMPUTATIONAL DETAILS

The ext-FPMD method follows the framework of the KSMD method and separates the motion of ions and electrons adiabatically based on the Born-Oppenheimer approximation [61]. The movement of ions is treated classically using Newton's second law, in which the Hellman-Feynman theorem [62] enables the calculation of forces on the ions. At the same time, the behavior of electrons is described quantum mechanically by solving the Kohn-Sham (KS) equations [33–35] $\hat{H}_{\rm KS}\psi_i = \epsilon_i\psi_i$, with

$$\hat{H}_{\rm KS} = -\tfrac{1}{2}\nabla^2 + V_H[n] + V_{xc}[n] + V_{ei}[n],$$

where the subscript i denotes the ith state, ψ_i is the wave function of the ith state, ϵ_i is the corresponding eigenenergy, V_H is the Hartree potential, V_{xc} is the exchange-correlation potential, V_{ei} is the electron-ion interaction potential, and n is the electronic density.

The main improvement of the ext-FPMD method [54] at high temperatures is the treatment of the wave functions of numerous high-energy-level electrons as plane waves because of the predominance of the kinetic energy in the total energy of these electrons. Hence, the contribution of high-energy-level electrons to electronic charge density, total energy, and entropy can be analytically described with the plane-wave approximation as

$$n_{\rm corr}(\mathbf{r}) = \frac{1}{\Omega}\int_{E_c}^{\infty} d\epsilon f(\epsilon)D(\epsilon),$$

$$E_{\rm corr} = \int_{E_c}^{\infty} d\epsilon f(\epsilon)D(\epsilon)(\epsilon - U_0),$$

and

$$S_{\rm corr} = -\int_{E_c}^{\infty} d\epsilon D(\epsilon)\{f(\epsilon)\ln f(\epsilon) + [1-f(\epsilon)]\ln[1-f(\epsilon)]\}.$$

Here, ϵ is the energy, Ω is the volume, U_0 is constant background energy, E_c is the lowest energy of high-energy-level electrons used in the plane-wave approximation, and $f(\epsilon)$ is the Fermi-Dirac distribution function. Similar to the free electron gas model, the density of states of the high-energy-level electrons is approximately adopted as

$$D(\epsilon) = \frac{\sqrt{2}\Omega}{\pi^2}\sqrt{\epsilon - U_0}.$$

All calculations are carried out with an implementation of the ext-FPMD method [54] based on the QUANTUM ESPRESSO package [63]. A periodic cubic box containing 8 Si atoms at temperature $T \geqslant 2.5\times10^5$ K and 24 Si atoms at lower temperatures is established to keep the size of the simulation system the same as that of the PIMC calculations [41]. For a given temperature and density, the time step to move the ions is determined by the empirical formula $\delta t = l/(40v_t)$, where l is the average distance between atoms and v_t is the average thermal velocity. Trajectories of the last 3000 steps are statistically analyzed to calculate the required physical quantities after the system has achieved thermal equilibrium. A shifted $2\times2\times2$ Monkhorst-Pack [64] k-point mesh is used to sample the Brillouin zone; 320 bands are explicitly included in calculations, of which the 80 bands at the top are used to determine the value of U_0, as required by the ext-FPMD method [54]. The Perdew-Wang parametrization [65] of the local-density approximation (LDA) and the Perdew-Burke-Ernzerhof parametrization [66] of the generalized gradient approximation (GGA) to the exchange-correlation functionals are employed. An all-electron pseudopotential for Si in the projected augmented-wave [67] format is generated using the ATOMPAW program [68,69]. The small-core cutoff radius is 0.5 bohr, and the corresponding plane-wave cutoff energy is 300 Ry. Two more FTXC functionals proposed by Karasiev, Sjostrom, Dufty, and Trickey [70] and Groth, Dornheim, Sjostrom, Malone, Foulkes, and Bonitz [71,72], denoted FTXC-KSDT and FTXC-GDSMFB, respectively, are also used to investigate the influence of FTXC functionals on EOS of warm dense Si.

The principal Hugoniot curve comes from the Rankine-Hugoniot relation $E_1 - E_0 = \frac{1}{2}(P_1+P_0)(V_0-V_1)$, where E is the internal energy, P is the pressure, and V is the specific volume. Subscripts 0 and 1 indicate the uncompressed and shocked states, respectively. The initial state of Si is a face-centered diamond-cubic lattice structure at $\rho_0 = 2.329$ g/cm^3, and the initial pressure $P_0 \approx 0$, while the initial energy E_0 depends on the choice of exchange-correlation functionals listed in the Supplemental Material [73]. The equation is solved with Newton's polynomial interpolation formula.

III. RESULTS AND DISCUSSION

A. Equation of state of silicon

We obtain a wide-range EOS for Si under various density and temperature conditions that range from a cold condensed matter state to warm or hot dense matter state (densities ρ in the range from solid ambient density $\rho_0 = 2.329$ g/cm^3 to eightfold solid density $\rho = 8\rho_0 = 18.632$ g/cm^3 and temperatures T in the range from 1.00×10^4 to 1.29×10^8 K) using the unified ext-FPMD method, assembled in the EOS table in the Supplemental Material [73]. The internal energy E and pressure P for ext-FPMD simulations with different exchange-correlation functionals are listed for different density and temperature conditions.

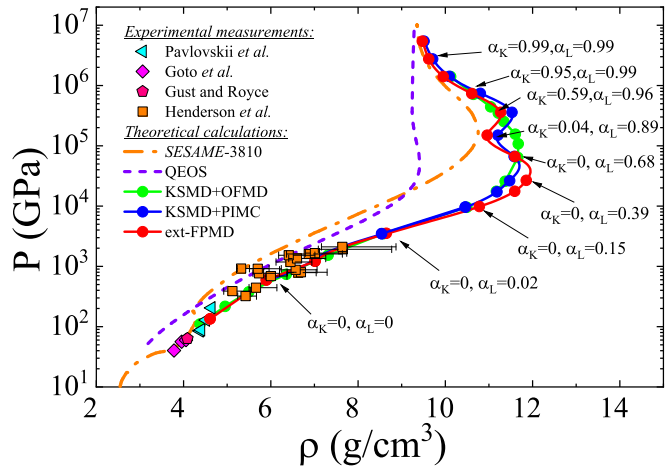

FIG. 1. Principal Hugoniot curve of Si calculated using the ext-FPMD method, compared with results from theoretical calculations and experimental measurements, including the combination of the KSMD and PIMC methods [41], the combination of the KSMD and OFMD methods [42,43], QEOS, SESAME-3810, and shock experiments by Pavlovskii [25], Gust and Royce [26], Goto *et al.* [27], and Henderson *et al.* [29].

Recently, Militzer and Driver [41] provided a set of the EOS and the shock Hugoniot curve for Si by combining the KSMD and PIMC methods, and then Hu *et al.* [42,43] established another first-principles EOS and shock Hugoniot curve for Si by combining the KSMD and the OFMD methods. Now, we show a detailed comparison of the above sets of EOSs using different first-principles methods.

Figure 1 displays the principal Hugoniots of Si obtained with several experimental measurements and theoretical calculations. Simulation results for the pressure P range from 10^2 to 10^7 GPa, including for the ext-FPMD method (red points), the combination of the KSMD and PIMC methods (blue points), and the combination of the KSMD and OFMD methods (green points). Lines under the first-principles EOS points are fitted curves using the interpolation code from Ref. [53]. Compared with existing experimental data, i.e., when $P < 2100$ GPa, our result and that of the KSMD method are in good agreement with experimental measurements by Pavlovskii [25], Gust and Royce [26], Goto *et al.* [27], and Henderson *et al.* [29]. Compared with commonly used EOS models, e.g., SESAME-3810 and quotidian equation of state (QEOS), all the results of the three first-principles methods converge with each other and manifest softened Hugoniots, which may have a considerable effect on the implosion process, which was systematically studied using radiation-hydrodynamic simulations in the work of Hu *et al.* [43].

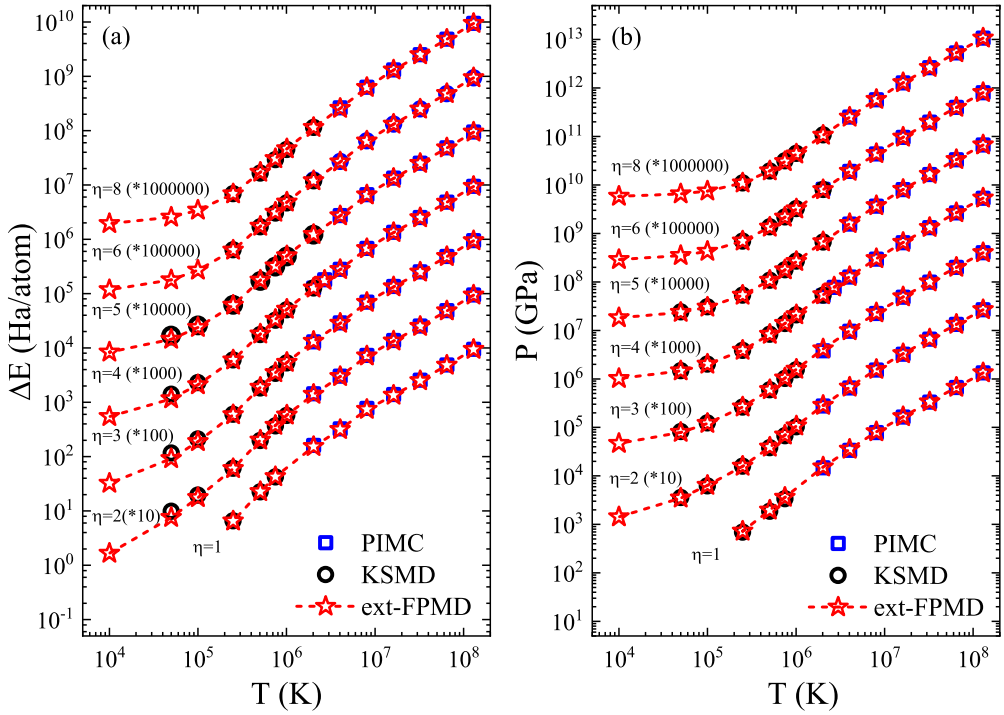

FIG. 2. Calculated EOS points of Si using the ext-FPMD method (red stars with dashed lines) compared with the KSMD (black circles) and PIMC (blue squares) methods [41], where (a) shows the energy differences $\Delta E = E - E_0$ and (b) shows pressure P. Energy differences in (a) and pressures in (b) at different η are multiplied by corresponding coefficients for a better display.

For the three first-principles calculations, different shapes and tendencies of the "bump" structures in principal Hugoniot curves, corresponding to the transition region, reflect different descriptions of inner shell electronic structure information in these methods. The process of the thermal ionization of multishell electrons from the outer shell to the inner shell can be quantitatively described by the variation of the average ionization ratios α_K and α_L of K and L shell electrons, which are extracted from the ext-FPMD method and displayed along the principal Hugoniot in Fig. 1. In the region of $P <\sim 2100$ GPa, i.e., the maximum pressure that existing experiments can reach, both α_K and α_L are nearly zero. With the increase of temperature and pressure, α_L increases, but α_K remains zero, indicating that only the L shell electrons are experiencing the process of ionization. When $\alpha_L > 0.39$, i.e., the L shell electrons are nearly half ionized, corresponding to the first or the lower turning point at the pressure of $\sim 2.7 \times 10^4$ GPa for the ext-FPMD and PIMC Hugoniots, α_K is still zero, and the L shell electrons dominate the thermal ionization process. After this point, the number of L shell electrons available to be ionized is smaller than that of already ionized ones, and the Hugoniot curves gradually move to the lower-density region. At $\alpha_L > 0.89$, i.e., when the L shell electrons are mostly ionized, α_K changes from zero, which means K shell electrons start to become ionized. In the following ionization process, the K shell electrons become available to be ionized, and thus, the Hugoniot curves move to the higher-density region again. When $\alpha_K \approx 0.59$, i.e., the K shell electrons are nearly half ionized, it reaches the second or upper turning point at a pressure of $\sim 3.6 \times 10^5$ GPa, meaning that ext-FPMD and PIMC results meet once again. Finally, the only remaining K shell electrons are entirely ionized, and the Hugoniot curves approach the ideal gas limit (density compression ratio $\eta = 4$ or $\rho = 9.316$ g/cm^3), converging with the commonly used EOS models, e.g., SESAME-3810 and QEOS.

As demonstrated above, the ionization of multishell electrons proceeds shell by shell along the shock Hugoniot curves. The deviations in the Hugoniot curves correspond to different physical approximation treatments for multishell electrons by analytic models and first-principles methods, reflecting the validity and reliability of those methods and derived results. The consistent bump structures in the Hugoniot curves from the ext-FPMD and PIMC methods provide access to an accurate description of the thermal ionization process of inner shell electrons, although the treatments of the motion of electrons by these two methods are pretty different. However, only one turning point at a pressure of 10^5 GPa appears in the OFMD method and SESAME-3810, and the corresponding pressure is 5×10^4 GPa in QEOS. Appropriate treatments of the shell structure effect in such methods are required to improve the completeness of physical methodologies and the accuracy of physical quantities. When $P > 10^6$ GPa, all results of first-principles methods and SESAME-3810 start to converge, and the gap between analytic models and first-principles methods vanishes because most electrons are ionized and the shell structure effect is negligible.

Figure 2 shows a point-by-point comparison of EOSs in a wide density-temperature range calculated using the ext-FPMD method (red stars) and the KSMD (black circles) and PIMC (blue squares) methods. The two sets of EOS points distribute in the same grid of density and temperature. To eliminate the effect of exchange-correlation functionals on a reference value for energy, Fig. 2(a) displays the internal energy difference between a high-temperature state and the

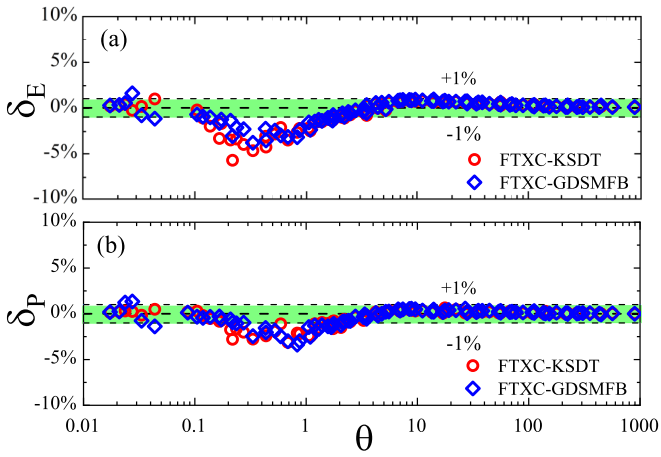

FIG. 3. Relative deviations of (a) the energy difference $\Delta E = E - E_0$ and (b) pressure P using the FTXC-KSDT and FTXC-GDSMFB functionals, taking the ZTXC-LDA functional as a reference.

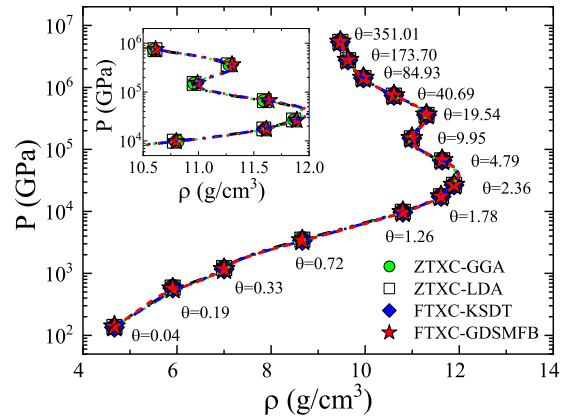

FIG. 4. Principal Hugoniots of Si using different types of exchange-correlation functionals, including ZTXC-GGA, ZTXC-LDA, FTXC-KSDT, and FTXC-GDSMFB. The inset shows a close-up near the maximum compression ratio.

initial uncompressed state in the Rankine-Hugoniot relation, defined as $\Delta E = E - E_0$. Conversely, Fig. 2(b) directly displays pressure P because the pressure of the initial state is negligible. Dashed lines connect EOS points with the same compression ratio $\eta = \rho/\rho_0$, which are multiplied by the same coefficient (after the multiplication sign in the parentheses), for a better display. There is hardly any visual difference between the points of these two sets of EOSs. Relative deviations of ΔE and P are within 2% except for individual points near the connecting region, which approaches the applicable boundaries of the KSMD and PIMC methods. We thus conclude that EOS data calculated using the ext-FPMD method and the combination of the KSMD and PIMC methods are overall convergent.

B. Effects of finite-temperature exchange correlation

We now show the effects of the FTXC on the EOS of warm dense Si. Using the calculated results with the zero-temperature exchange correlation (ZTXC) of the LDA functional as a reference, we investigate relative deviations of EOSs between ZTXC and different types of FTXC as a function of the electron degeneracy parameter $\theta = T/T_F$, where $T_F \propto \rho^{2/3}$ is the Fermi temperature. Temperature and density effects are simultaneously included in θ with the point-by-point comparison. To quantitatively investigate the effect of different exchange-correlation functionals on the EOS, we define the relative deviation of the energy difference ΔE in the Rankine-Hugoniot relation as $\delta_E = (\Delta E_{\mathrm{FTXC}} - \Delta E_{\mathrm{ZTXC}})/\Delta E_{\mathrm{ZTXC}}$, where subscript after ΔE represents the EOS data obtained with the respective exchange-correlation functional. Similarly, the relative deviation of the pressure is directly defined as $\delta_P = (P_{\mathrm{FTXC}} - P_{\mathrm{ZTXC}})/P_{\mathrm{ZTXC}}$.

Figure 3 displays the relative deviation of the energy difference and pressure with the FTXC-KSDT and FTXC-GDSMFB functionals as a function of θ, shown as red circles and blue squares, respectively. The overall trends of δ_E and δ_P varying with θ using the FTXC-KSDT and FTXC-GDSMFB functionals are basically the same, although individual points separate because of the subtle differences between the analytic formulas in the two FTXC functionals. With the increase of θ, the distribution of these points can be divided into three parts, in accordance with the horizontal reference lines $\pm 1\%$. In the first part, the majority points of δ_E and δ_P are located in the green region between the two horizontal reference lines when $\theta < 0.1$, indicating that the effect of FTXC is insignificant in this region and the results for FTXC and ZTXC converge. In the second part, both δ_E and δ_P from FTXC-KSDT and FTXC-GDSMFB drop down to the minimum value of $\sim -5\%$ at $\theta \sim 1$, then jump onto the -1% horizontal reference line at $\theta \approx 3$, and, eventually, vary from -1% to $+1\%$ when $3 < \theta < 10$. In the third part, both δ_E and δ_P gradually approach zero when $\theta > 10$, which indicates the results for FTXC and ZTXC converge again because exchange-correlation energy accounts for little of the total energy owing to the feature of entirely ionized plasma.

Taking both δ_E and δ_P into consideration, the influence of FTXC on the EOS of Si is worth paying attention to when $0.1 < \theta < 10$, i.e., in the warm dense matter regime. One should be able to describe exchange-correlation interactions accurately using these well-designed FTXC functionals in such a system with partial ionization and partial degeneracy.

Figure 4 displays principal Hugoniots calculated with the FTXC-KSDT and FTXC-GDSMFB functionals, compared with results calculated with the ZTXC of the LDA and GGA functionals. Calculated Hugoniot points with different exchange-correlation functionals coincide in an extensive pressure range, especially for states below 10^4 GPa or above 10^6 GPa. The majority deviation of Hugoniots appears in the region near the two turning points from $\theta = 1.26$ to $\theta = 19.54$, i.e., the warm dense matter regime, displayed in the inset of Fig. 4. It is consistent with the tendency of the effects of FTXC functionals on the EOS displayed in Fig. 3. We note that Hugoniots with the two FTXC functionals are both slightly softened compared with those with ZTXC functionals, indicating a larger maximum compression ratio, as shown in the inset of Fig. 4. The above shows that fully considering the effect of FTXC functionals is necessary for obtaining high-precision thermodynamics parameters, especially in the

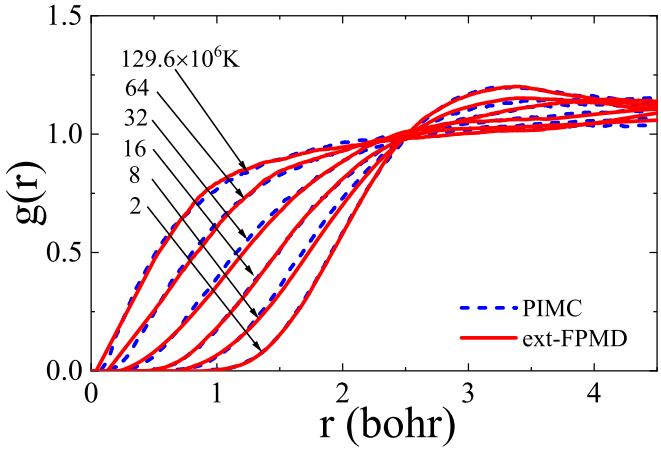

FIG. 5. Radial distribution functions of Si ions at fourfold density and various temperatures, calculated using the ext-FPMD method (solid red lines) and the PIMC method (blue dashed lines).

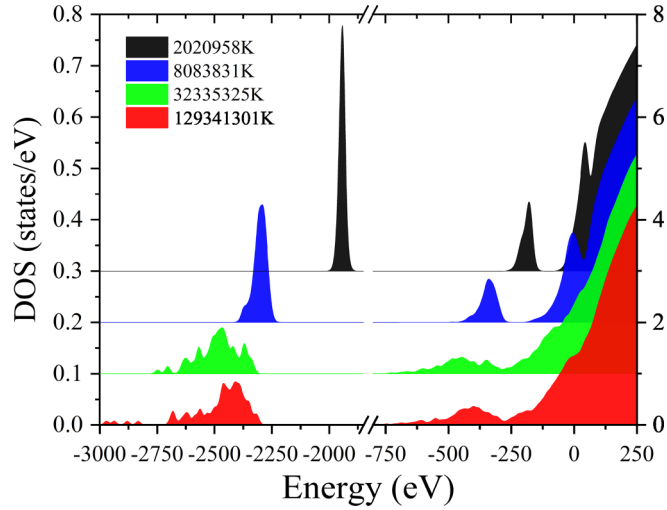

FIG. 6. Density of electronic states of Si at fourfold density and various temperatures, calculated using the ext-FPMD method.

warm dense matter regime. The origin of minor deviations between the two sets of EOSs calculated using the existing two types of FTXC functionals should attract interest with regard to understanding the effect of FTXC functionals and improving the accuracy of current first-principles simulations.

C. Microscopic structure information

Microscopic structure information, including the ionic RDF and electronic DOS, obtained from first-principles methods provides useful information to understand physical processes corresponding to the variation of thermodynamics quantities. Meanwhile, the convergence of microscopic structure information calculated with the above first-principles methods based on different physical approximations reflects the consistency and reliability of these methods.

Figure 5 displays ionic RDFs of Si at fourfold density calculated using ext-FPMD (solid red lines) and PIMC (blue dashed lines) while varying temperature. Numbers next to each RDF indicate temperatures in units of 10^6 K. There is a hardly perceivable distinction between the solid red line and blue dashed line, indicating that the two methods give a consistent description of interactions between the partially ionized particles. Figure 5 shows that only one peak structure appears in the RDFs at $r \approx 3.5$ bohr at relatively low temperatures. With the increase of temperature, the values of the RDFs at short and long distances systematically rise and fall, respectively, and both approach the ideal-gas limit of $g(r) = 1$, which indicates that the increase of kinetic energy leads to a tendency of the system to become an ideal gas. We can clearly observe the evolution process of the state of Si from warm dense matter to an ideal plasma with the increase of temperature.

Another main advantage of ext-FPMD is that it can provide the relevant structure information produced by the retained electronic wave function. We obtain the DOS of Si at fourfold density and temperatures T from 2×10^6 to 129×10^6 K using the ext-FPMD method, displayed in Fig. 6. To better display the details, the DOSs of inner shell electrons and other electrons use different scales on the left and right axes, and the DOSs at different temperatures are distinguished by shifting up one unit. Figure 6 shows that the distribution of the K shell electronic state in the DOS, energetically separated from other electrons at relatively low energy, smears out and moves toward the low-energy region with the increase of temperature. This is because of the increase of the valance state of Si ions due to the thermal ionization process along the Hugoniot curve. For electronic states at relatively high energy, with the increase of temperature, the same smearing out and moving process occurs, and the overlapping of electronic states when $T > 32335325$ K is the result of intense thermal fluctuations at such extremely high temperatures.

From the microscopic structure information described above, one can obtain more material properties, including electronic conductivity, thermal conductivity, opacity, and the x-ray absorption spectrum, and then carry out further experiments in the future, which will help us deepen the understanding of physical effects at extremely high temperatures.

IV. CONCLUDING REMARKS

We reported a set of EOSs and principal Hugoniots of Si at pressures varying from $\sim 10^2$ GPa to above 10^7 GPa and temperatures varying from $\sim 10^4$ K to above 10^8 K using the unified method of ext-FPMD instead of a combination technique. A point-by-point comparison of EOS data and RDFs calculated using ext-FPMD and PIMC showed the consistency of macroscopic and microscopic quantities obtained with different first-principles methods based on different physical approximations. This mutually verifies the accuracy of the most advanced first-principles methods so far, i.e., ext-FPMD and PIMC, and thus creates a standard benchmark for the feasibility and accuracy of new theoretical methods in the future. In addition, the study of the effects of FTXC emphasized the importance and necessity of FTXC functionals for the EOS, especially for warm dense matter.

Following the findings concluded above, one can further study the effects on the EOS from a higher order of

exchange-correlation functionals along Jacob's ladder [74], including the strongly constrained and appropriately normed meta-GGA, and hybrid HSE functional, as well as FTXC functionals beyond the LDA [75]. Current studies [76–79] have already achieved remarkable results and deepened the understanding of the physical origin of minor deviations caused by different exchange-correlation functionals. Even so, the size of simulated systems is limited by existing computational capability, considering the large numbers of parallel tasks need to establish a first-principles database. We note that recent works on interatomic potentials of Si may lead to a possible approach to avoid the overwhelming computational costs of the size effect in the pair potential model [80] and machine learning model with full consideration of quantum mechanical effects [81–83]. Meanwhile, the relativistic and radiation effects may play essential roles in the EOS at extremely high temperatures [53,84,85], and how significantly the modified EOS database affects radiation-hydrodynamic models is also a scientific issue worth studying.

ACKNOWLEDGMENTS

This work is financially supported by the NSFC (Grants No. 11904401 and No. 12105209), the Science Challenging Program (Grant No. TZ2016001), and the Fundamental Research Funds for the Central Universities (Grant No. WUT:2021IVA067).

[1] A. Mujica, A. Rubio, A. Muñoz, and R. J. Needs, Rev. Mod. Phys. **75**, 863 (2003).
[2] D. Alfè, M. J. Gillan, M. D. Towler, and R. J. Needs, Phys. Rev. B **70**, 214102 (2004).
[3] R. G. Hennig, A. Wadehra, K. P. Driver, W. D. Parker, C. J. Umrigar, and J. W. Wilkins, Phys. Rev. B **82**, 014101 (2010).
[4] Q. Wang, B. Xu, J. Sun, H. Liu, Z. Zhao, D. Yu, C. Fan, and J. He, J. Am. Chem. Soc. **136**, 9826 (2014).
[5] J. Wu, H. Gao, K. Xia, D. Xing, and J. Sun, Appl. Phys. Lett. **111**, 173904 (2017).
[6] R. Paul, S. X. Hu, and V. V. Karasiev, Phys. Rev. Lett. **122**, 125701 (2019).
[7] L. Rapp, B. Haberl, C. J. Pickard, J. E. Bradby, E. G. Gamaly, J. S. Williams, and A. V. Rode, Nat. Commun. **6**, 7555 (2015).
[8] J.-F. Lin, D. L. Heinz, A. J. Campbell, J. M. Devine, and G. Shen, Science **295**, 313 (2002).
[9] Z. Mao, J.-F. Lin, J. Liu, A. Alatas, L. Gao, J. Zhao, and H.-K. Mao, Proc. Natl. Acad. Sci. USA **109**, 10239 (2012).
[10] J. K. Wicks, R. F. Smith, D. E. Fratanduono, F. Coppari, R. G. Kraus, M. G. Newman, J. R. Rygg, J. H. Eggert, and T. S. Duffy, Sci. Adv. **4**, 23 (2018).
[11] W.-P. Hsieh, A. F. Goncharov, S. Labrosse, N. Holtgrewe, S. S. Lobanov, I. Chuvashova, F. Deschamps, and J.-F. Lin, Nat. Commun. **11**, 1 (2020).
[12] H. Huang, L. Fan, X. Liu, F. Xu, Y. Wu, G. Yang, C. Leng, Q. Wang, J. Weng, X. Wang, L. Cai, and Y. Fei, Nat. Commun. **13**, 616 (2022).
[13] A. Benuzzi-Mounaix, S. Mazevet, A. Ravasio, T. Vinci, A. Denoeud, M. Koenig, N. Amadou, E.k Brambrink, F. Festa, A. Levy, M. Harmand, S. Brygoo, G. Huser, V. Recoules, J. Bouchet, G. Morard, F. Guyot, T. Resseguier, K. Myanishi, N. Ozaki, F. Dorchies, J. Gaudin, P. M. Leguay, O. Peyrusse, O. Henry, D. Raffestin, S. L. Pape, R. Smith and R. Musella, Phys. Scr. **T161**, 014060 (2014).
[14] M. Bethkenhagen, B. B. L. Witte, M. Schörner, G. Röpke, T. Döppner, D. Kraus, S. H. Glenzer, P. A. Sterne, and R. Redmer, Phys. Rev. Res. **2**, 023260 (2020).
[15] A. Ravasio, M. Bethkenhagen, J.-A. Hernandez, A. Benuzzi-Mounaix, F. Datchi, M. French, M. Guarguaglini, F. Lefevre, S. Ninet, R. Redmer, and T. Vinci, Phys. Rev. Lett. **126**, 025003 (2021).
[16] M. D. Knudson and M. P. Desjarlais, Phys. Rev. Lett. **118**, 035501 (2017).
[17] M. C. Marshall, A. E. Lazicki, D. Erskine, R. A. London, D. E. Fratanduono, P. M. Celliers, J. H. Eggert, F. Coppari, D. C. Swift, P. A. Sterne, H. D. Whitley, and J. Nilsen, Phys. Rev. B **99**, 174101 (2019).
[18] J. Lindl, Phys. Plasmas **2**, 3933 (1995).
[19] X. T. He, J. W. Li, Z. F. Fan, L. F. Wang, J. Liu, K. Lan, J. F. Wu, and W. H. Ye, Phys. Plasmas **23**, 082706 (2016).
[20] L. Li, L. Zhang, S. Jiang, L. Guo, B. Qing, Z. Li, J. Zhang, J. Yang, and Y. Ding, Appl. Phys. Lett. **104**, 054106 (2014).
[21] K. Du, M. Liu, T. Wang, X. He, Z. Wang, and J. Zhang, Matter Radiat. Extremes **3**, 135 (2018).
[22] M. W. C. Dharma-wardana, Phys. Rev. Lett. **101**, 035002 (2008).
[23] S. M. Vinko, O. Ciricosta, B. I. Cho, K. Engelhorn, H.-K. Chung, C. R. D. Brown, T. Burian, J. Chalupský, R. W. Falcone, C. Graves *et al.*, Nature (London) **482**, 59 (2012).
[24] M. Bonitz, T. Dornheim, Z. A. Moldabekov, S. Zhang, P. Hamann, H. Kählert, A. Filinov, K. Ramakrishna, and J. Vorberger, Phys. Plasmas **27**, 042710 (2020).
[25] M. N. Pavlovskii, Sov. Phys. Solid State **9**, 2514 (1968).
[26] W. H. Gust and E. B. Royce, J. Appl. Phys. **42**, 1897 (1971).
[27] T. Goto, T. Sato, and Y. Syono, Jpn. J. Appl. Phys. **21**, L369 (1982).
[28] A. Loveridge-Smith, A. Allen, J. Belak, T. Boehly, A. Hauer, B. Holian, D. Kalantar, G. Kyrala, R. W. Lee, P. Lomdahl, M. A. Meyers, D. Paisley, S. Pollaine, B. Remington, D. C. Swift, S. Weber, and J. S. Wark, Phys. Rev. Lett. **86**, 2349 (2001).
[29] B. J. Henderson, M. C. Marshall, T. R. Boehly, R. Paul, C. A. McCoy, S. X. Hu, D. N. Polsin, L. E. Crandall, M. F. Huff, D. A. Chin, J. J. Ruby, X. Gong, D. E. Fratanduono, J. H. Eggert, J. R. Rygg, and G. W. Collins, Phys. Rev. B **103**, 094115 (2021).
[30] E. J. Reed, J. D. Joannopoulos, and L. E. Fried, in *Shock Compression of Condensed Matter - 2001: 12th APS Topical Conference*, AIP Conf. Proc. No. 620 (AIP, Melville, NY, 2002), pp. 343–346
[31] I. I. Oleynik, S. V. Zybin, M. L. Elert, and C. T. White, in *Shock Compression of Condensed Matter - 2005: Proceedings of the Conference of the American Physical Society Topical Group on Shock Compression of Condensed Matter*, AIP Conf. Proc. No. 845 (AIP, Melville, NY, 2006), pp. 413–416.

[32] G. Mogni, A. Higginbotham, K. Gaál-Nagy, N. Park, and J. S. Wark, Phys. Rev. B **89**, 064104 (2014).
[33] P. Hohenberg and W. Kohn, Phys. Rev. **136**, B864 (1964).
[34] W. Kohn and L. J. Sham, Phys. Rev. **140**, A1133 (1965).
[35] N. D. Mermin, Phys. Rev. **137**, A1441 (1965).
[36] F. Lambert, J. Clérouin, and G. Zérah, Phys. Rev. E **73**, 016403 (2006).
[37] D. M. Ceperley, Rev. Mod. Phys. **67**, 279 (1995).
[38] B. Militzer and D. M. Ceperley, Phys. Rev. Lett. **85**, 1890 (2000).
[39] D. C. Swift, G. J. Ackland, A. Hauer, and G. A. Kyrala, Phys. Rev. B **64**, 214107 (2001).
[40] O. Strickson and E. Artacho, Phys. Rev. B **93**, 094107 (2016).
[41] B. Militzer and K. P. Driver, Phys. Rev. Lett. **115**, 176403 (2015).
[42] S. X. Hu, B. Militzer, L. A. Collins, K. P. Driver, and J. D. Kress, Phys. Rev. B **94**, 094109 (2016).
[43] S. X. Hu, R. Gao, Y. Ding, L. A. Collins, and J. D. Kress, Phys. Rev. E **95**, 043210 (2017).
[44] S. X. Hu, B. Militzer, V. N. Goncharov, and S. Skupsky, Phys. Rev. Lett. **104**, 235003 (2010).
[45] A. J. White and L. A. Collins, Phys. Rev. Lett. **125**, 055002 (2020).
[46] C. Wang, X.-T. He, and P. Zhang, Phys. Rev. Lett. **106**, 145002 (2011).
[47] Y. Ke, F. Libisch, J. Xia, L.-W. Wang, and E. A. Carter, Phys. Rev. Lett. **111**, 066402 (2013).
[48] T. G. White, S. Richardson, B. J. B. Crowley, L. K. Pattison, J. W. O. Harris, and G. Gregori, Phys. Rev. Lett. **111**, 175002 (2013).
[49] T. Sjostrom and J. Daligault, Phys. Rev. Lett. **113**, 155006 (2014).
[50] T. Sjostrom and S. Crockett, Phys. Rev. B **92**, 115104 (2015).
[51] B. Militzer, Phys. Rev. Lett. **97**, 175501 (2006).
[52] K. P. Driver and B. Militzer, Phys. Rev. Lett. **108**, 115502 (2012).
[53] B. Militzer, F. González-Cataldo, S. Zhang, K. P. Driver, and F. Soubiran, Phys. Rev. E **103**, 013203 (2021).
[54] S. Zhang, H. Wang, W. Kang, P. Zhang, and X. T. He, Phys. Plasmas **23**, 042707 (2016).
[55] C. Gao, S. Zhang, W. Kang, C. Wang, P. Zhang, and X. T. He, Phys. Rev. B **94**, 205115 (2016).
[56] A. Blanchet, M. Torrent, and J. Clerouin, Phys. Plasmas **27**, 122706 (2020).
[57] X. Liu, X. Zhang, C. Gao, S. Zhang, C. Wang, D. Li, P. Zhang, W. Kang, W. Zhang, and X. T. He, Phys. Rev. B **103**, 174111 (2021).
[58] A. Blanchet, J. Clérouin, M. Torrent, and F. Soubiran, Comput. Phys. Commun. **271**, 108215 (2022).
[59] A. Blanchet, F. Soubiran, M. Torrent, and J. Clérouin, Contrib. Plasma Phys. **62**, e202100234 (2022).
[60] P. Hollebon and T. Sjostrom, Phys. Rev. B **105**, 235114 (2022).
[61] G. Kresse and J. Hafner, Phys. Rev. B **47**, 558 (1993).
[62] R. M. Martin, *Electronic Structure: Basic Theory and Practical Methods* (Cambridge University Press, Cambridge, 2004).
[63] P. Giannozzi, S. Baroni, N. Bonini, M. Calandra, R. Car, C. Cavazzoni, D. Ceresoli, G. L. Chiarotti, M. Cococcioni, I. Dabo *et al.*, J. Phys.: Condens. Matter **21**, 395502 (2009).
[64] H. J. Monkhorst and J. D. Pack, Phys. Rev. B **13**, 5188 (1976).
[65] J. P. Perdew and Y. Wang, Phys. Rev. B **45**, 13244 (1992).
[66] J. P. Perdew, K. Burke, and M. Ernzerhof, Phys. Rev. Lett. **77**, 3865 (1996).
[67] P. E. Blöchl, Phys. Rev. B **50**, 17953 (1994).
[68] N. A. W. Holzwarth, A. R. Tackett, and G. E. Matthews, Comput. Phys. Commun. **135**, 329 (2001).
[69] M. Torrent, N. Holzwarth, F. Jollet, D. Harris, N. Lepley, and X. Xu, Comput. Phys. Commun. **181**, 1862 (2010).
[70] V. V. Karasiev, T. Sjostrom, J. Dufty, and S. B. Trickey, Phys. Rev. Lett. **112**, 076403 (2014).
[71] T. Schoof, S. Groth, J. Vorberger, and M. Bonitz, Phys. Rev. Lett. **115**, 130402 (2015).
[72] S. Groth, T. Dornheim, T. Sjostrom, F. D. Malone, W. M. C. Foulkes, and M. Bonitz, Phys. Rev. Lett. **119**, 135001 (2017).
[73] See Supplemental Material at http://link.aps.org/supplemental/10.1103/PhysRevB.107.165150 for complete EOS data for Si.
[74] J. P. Perdew and K. Schmidt, in *Density Functional Theory and Its Application to Materials*, AIP Conf. Proc. No. 577 (AIP, Melville, NY, 2001), pp. 1–20.
[75] V. V. Karasiev, J. W. Dufty, and S. B. Trickey, Phys. Rev. Lett. **120**, 076401 (2018).
[76] T. S. Tan, J. J. Kas, and J. J. Rehr, Phys. Rev. B **98**, 115125 (2018).
[77] V. V. Karasiev, S. X. Hu, M. Zaghoo, and T. R. Boehly, Phys. Rev. B **99**, 214110 (2019).
[78] K. Ramakrishna, T. Dornheim, and J. Vorberger, Phys. Rev. B **101**, 195129 (2020).
[79] K. Luo, V. V. Karasiev, and S. B. Trickey, Phys. Rev. B **101**, 075116 (2020).
[80] M. W. C. Dharma-wardana, Phys. Rev. E **86**, 036407 (2012).
[81] A. P. Bartók, S. De, C. Poelking, N. Bernstein, J. R. Kermode, G. Csányi, and M. Ceriotti, Sci. Adv. **3**, e1701816 (2017).
[82] A. P. Bartók, J. Kermode, N. Bernstein, and G. Csányi, Phys. Rev. X **8**, 041048 (2018).
[83] Q. Zeng, B. Chen, X. Yu, S. Zhang, D. Kang, H. Wang, and J. Dai, Phys. Rev. B **105**, 174109 (2022).
[84] H. Eschrig and V. D. P. Servedio, J. Comput. Chem. **20**, 23 (1999).
[85] R. Piron and T. Blenski, Phys. Rev. E **83**, 026403 (2011).